CrossMark

J. Fluid Mech. (2016), *vol.* 795, *pp.* 652–670. © Cambridge University Press 2016
doi:10.1017/jfm.2016.176

Crow instability: nonlinear response to the linear optimal perturbation

Holly G. Johnson[1,†], **Vincent Brion**[1] **and Laurent Jacquin**[1]

[1]Fundamental and Experimental Aerodynamics Department, ONERA, 8 rue des Vertugadins, 92190 Meudon, France

(Received 23 July 2015; revised 2 February 2016; accepted 1 March 2016; first published online 19 April 2016)

The potential for anticipated destruction of a counter-rotating vortex pair using the linear optimal perturbation of the Crow instability is assessed. Direct numerical simulation is used to study the development of the Crow instability and the subsequent evolution of the flow up to 30 characteristic times at a circulation-based Reynolds number of 1000. The conventional development of the instability leads to multiple contortions of the vortices including the linear growth of sinusoidal deformation, vortex linking and the formation of vortex rings. A new evolution stage is identified, succeeding this well-established sequence: the vortex rings undergo periodic oscillation. Two complete periods are simulated during which the vortical system is hardly altered, thereby demonstrating the extraordinary resilience of the vortices. The possibility of preventing these dynamics using the linear optimal perturbation of the Crow instability, the adjoint mode, is analysed. By appropriately setting the forcing amplitude, the lifetime of the vortices until their loss of coherence is reduced to approximately 13 characteristic times, which is less than half that of the natural Crow behaviour observed with infinitesimal forcing. The dynamics of the flow induced by the linear optimal perturbation that enable this result are connected to processes already known to efficiently alter vortical flows, in particular transient growth and four-vortex dynamics.

Key words: vortex dynamics, vortex flows, vortex instability

1. Introduction

The increasing demand for air transport across the world has led to saturation in many major airports. Take-off and landing rhythms are limited by a safety interval imposed to avoid the danger of encountering an aircraft wake. Taking the form of a counter-rotating vortex pair, this powerful wake generates a rotating force that could tip a following aircraft. This danger is also encountered at cruising level and represents a major concern for air traffic control. The understanding and control of these coherent structures is therefore of paramount importance and has been the aim of many studies for several decades.

The optimal perturbation is the perturbation that generates maximum growth of perturbation energy over a certain period of time and therefore constitutes the ideal

† Email address for correspondence: hollyjohnson90@gmail.com

https://doi.org/10.1017/jfm.2016.176 Published online by Cambridge University Press

perturbation for disrupting a flow. Many optimal perturbation studies have been carried out on various flow configurations. In the case of an isolated vortex, Antkowiak & Brancher (2004) and more recently Pradeep & Hussain (2006) determined the linear optimal perturbations for azimuthal wavenumbers $m = 1$ and $m = 1 \ldots 4$, respectively. In particular the $m = 1$ mode with wavenumber $ka = 1.4$ leads to significant transient growth in this otherwise linearly stable flow. Farrell (1988) established that the linear optimal perturbation of a particular flow corresponds to the adjoint of the most unstable mode of the flow. Brion, Sipp & Jacquin (2007) applied this principle to a counter-rotating vortex pair. The dominant instability of this configuration is the Crow instability (Crow 1970) which induces symmetrical sinusoidal displacement of the vortex cores. The linear optimal perturbation corresponding to the Crow instability established by Brion *et al.* (2007) takes the form of vorticity sheets concentrated close to the plane separating the two vortices and produces considerable transient growth before reaching the classic linear Crow instability behaviour.

It has been shown by many that when an isolated vortex is subjected to external perturbation, secondary helical structures form, wrapping around the core in a manner that is very similar to that of the linear optimal. Melander & Hussain (1993), Miyazaki & Hunt (2000) and Marshall & Beninati (2005) studied the reaction of a vortex to fine-scale turbulence using direct numerical simulation (DNS), and Fontane, Brancher & Fabre (2008) continuously stimulated a vortex using stochastic forcing. In all of these studies the emergence of the linear optimal was observed. Whatever the form of the perturbation, the modes corresponding to the linear optimal are preferentially excited through the interaction with the vortex. Although the initial perturbation development is linear, once secondary structures are formed it is possible they will interact and the subsequent evolution will be nonlinear. It is therefore legitimate to pose the question, what happens to linear optimal perturbations when the nonlinearities become non-negligible. Another question of importance is that of the effect of a finite initial amplitude of the optimal perturbation and how it would influence the evolution of the flow. Such questions cannot be answered in a linear framework and become important when the practicality of the approach is questioned. It should be noted that the feasibility of the linear optimal perturbation of the Crow instability occurring or being generated in a real vortex system is not addressed in this study which remains at the theoretical level, but this should be approached at a later stage.

The method used in this paper, initialising a nonlinear DNS with the linear optimal mode, has been applied in previous works. Hussain, Pradeep & Stout (2011) studied the nonlinear evolution of the linear optimal mode of an isolated vortex and observed that moderate initial perturbation amplitudes at a high enough Reynolds number could trigger core transition. Shaeffer & Le Dizès (2010) studied the nonlinear evolution of the elliptic instability on a single strained vortex and a pair of counter-rotating vortices. Schmid & Henningson (2001) showed that the linear optimal perturbation with finite initial amplitudes can generate laminar–turbulent transition in normal-mode stable shear flows.

The aim of this paper is to study the nonlinear response to the linear optimal perturbation of a counter-rotating vortex pair determined by Brion *et al.* (2007) using DNS. The paper is organised in the following manner. The methods used to carry out the DNS and to obtain the linear perturbation mode are outlined (§ 2). A preliminary study of the long-term behaviour of the Crow instability with infinitesimal initial amplitude is carried out to provide a reference for the following analysis (§ 3). The nonlinear response to the linear optimal perturbation introduced with growing

https://doi.org/10.1017/jfm.2016.176 Published online by Cambridge University Press

initial amplitudes is then studied and compared with the reference case (§ 4). Finally the physical mechanisms involved in the accelerated decay of the vortex pair are described (§ 5).

2. Governing equations

The flow is governed by the incompressible Navier–Stokes equations:

$$\boldsymbol{\nabla} \cdot \boldsymbol{u} = 0 \tag{2.1}$$

$$\partial_t \boldsymbol{u} + (\boldsymbol{u} \cdot \boldsymbol{\nabla})\boldsymbol{u} = -\boldsymbol{\nabla} p + \nu \nabla^2 \boldsymbol{u}. \tag{2.2}$$

Decomposing the velocity and pressure of the flow into components corresponding to the base flow and to a small perturbation, $\boldsymbol{u} = \boldsymbol{U} + \epsilon \boldsymbol{u}'$, $p = P + \epsilon p'$ with $\epsilon \ll 1$ and linearising the equations around the base flow yields the linearised Navier–Stokes equations given here at first order of ϵ:

$$\boldsymbol{\nabla} \cdot \boldsymbol{u}' = 0 \tag{2.3}$$

$$\partial_t \boldsymbol{u}' + (\boldsymbol{u}' \cdot \boldsymbol{\nabla})\boldsymbol{U} + (\boldsymbol{U} \cdot \boldsymbol{\nabla})\boldsymbol{u}' = -\boldsymbol{\nabla} p' + \nu \nabla^2 \boldsymbol{u}'. \tag{2.4}$$

The base flow of the simulation is composed of a pair of counter-rotating Lamb–Oseen vortices, with initial azimuthal velocity U_θ defined as

$$U_\theta(r) = \frac{\Gamma}{2\pi r}(1 - \mathrm{e}^{-r^2/a^2}), \tag{2.5}$$

with Γ the circulation of the vortex.

All results are rendered non-dimensional by the initial distance separating the vortices b and the drift velocity of the vortex pair through mutual induction $U_{drift} = \Gamma/2\pi b$. The characteristic evolution time of the dipole is the time it takes to descend a distance equal to b through mutual induction, $\tau = b/U_{drift} = 2\pi b^2/\Gamma$. The resulting Reynolds number is $Re = \Gamma/2\pi\nu$ with ν the kinematic viscosity of the fluid. In this case, the Reynolds number is taken to be $Re = 1000$ and the initial aspect ratio of the vortex pair is $a/b = 0.18$. In order to avoid the transient phase due to the adaptation of the Lamb–Oseen vortex pair to the Navier–Stokes equations, the base flow is time-stepped forward by several reference times ($t \approx 8$) before embarking on the perturbation analysis. The details of this method are described by Sipp (1999). During the linear simulations to obtain the linear optimal perturbation the base flow is 'frozen'. This is valid as long as the viscous timescale is large compared with the timescale of the perturbation dynamics. The timescale of the viscous diffusion of a vortex being $t_\nu = 2\pi a^2/\nu$, the ratio of these two timescales $t_\nu/\tau = (a/b)^2 Re$ is indeed large.

As the wavelength of the most unstable Crow mode is around $\lambda_z = 7b$, the simulations are carried out on a mesh of extent $[-L_x/2, L_x/2] \times [-L_y/2, L_y/2] \times [-L_z/2, L_z/2]$ with $L_x = 9.6b$, $L_y = 10.8b$, $L_z = 7b$ in order to calculate one complete wavelength of the instability. Cartesian coordinates (x, y, z) are used throughout the study. The largest divisions in each direction are $\Delta x_{max}/b \approx 0.025$, $\Delta y_{max}/b \approx 0.03$, $\Delta z_{max}/b \approx 0.02$. The DNS is carried out using the incompressible Navier–Stokes solver Nek5000 (Fischer, Lottes & Kerkemeier 2008), which is based on a spectral elements method. The computational domain is split into N_e^3 uniformly distributed elements with $N_e = 70$, containing $N_{GLL} = 8$ Gauss–Lobatto–Legendre

https://doi.org/10.1017/jfm.2016.176 Published online by Cambridge University Press

(GLL) points in each direction. The largest mesh interval is given by $\Delta d_{max} = \pi L_d/2(N_{GLL}-1)N_e$ with $d \in x, y, z$.

Although the flow studied in this paper is initially laminar, the nature of the resulting dynamics is unknown and potentially turbulent. Therefore, it is judicious to create a mesh that can handle a turbulent flow calculation were it to materialise. The mesh must be fine enough to capture the Kolmogorov dissipation scale $\lambda_{Kolm} = Re^{-3/4}b \approx 6 \times 10^{-3}$ and the shear layer scale at the leading hyperbolic point $\delta = (2\pi b^2\nu/3^{1/2}\Gamma)^{1/2} \approx 2.5 \times 10^{-2}$ determined here for a point vortex model. The contribution of eddies of scale $l \leqslant 5\lambda_{Kolm}$ is negligible (Pope 2000), and therefore the current mesh, designed on this threshold, is sufficient. As confirmation a test was carried out using half the number of elements for the same domain size, which gave close to identical results, with less than 3 % difference between the values of the circulation at $t = 10$. Similarly the adequacy of the domain size was validated using a mesh twice as large, keeping the same number of elements and GLL points. Boundary conditions in the axial direction (z) are periodic. In order to compensate for the descent of the vortex pair through mutual induction a vertical velocity is imposed in the domain. Therefore, the boundary conditions on the negative and positive y-borders are inflow and outflow, respectively. Finally in the spanwise direction symmetrical conditions are imposed.

Farrell (1988) demonstrated that the linear optimal perturbation of a flow is the adjoint of the most unstable mode of the flow. The adjoint of the most unstable Crow mode is determined by solving the adjoint linearised Navier–Stokes equations. The adjoint $\tilde{A}$ of an operator A is defined as $(\boldsymbol{x}, A\boldsymbol{y}) = (\tilde{A}\boldsymbol{x}, \boldsymbol{y}) + \text{b.c.}$ with $\boldsymbol{x}$ and $\boldsymbol{y}$ vectors, $(\cdot, \cdot)$ the scalar product and b.c. meaning boundary conditions. Applying this definition to the operator corresponding to the linearised Navier–Stokes equations gives the adjoint equations:

$$\boldsymbol{\nabla} \cdot \tilde{\boldsymbol{u}}' = 0 \tag{2.6}$$

$$\partial_t \tilde{\boldsymbol{u}}' + (\tilde{\boldsymbol{u}}' \cdot \boldsymbol{\nabla})\boldsymbol{U} - (\boldsymbol{U} \cdot \boldsymbol{\nabla})\tilde{\boldsymbol{u}}' = -\boldsymbol{\nabla}\tilde{p}' + \nu\nabla^2\tilde{\boldsymbol{u}}'. \tag{2.7}$$

The initial velocity field for each DNS simulation described in this paper is expressed as $\boldsymbol{u}_\epsilon(0) = \boldsymbol{U} + \epsilon\|\boldsymbol{U}\|\boldsymbol{u}_0'$ with $\boldsymbol{u}_0'$ the normalised perturbation velocity field (the adjoint Crow mode is taken here). Once started the simulation yields the flow field $\boldsymbol{u}_\epsilon(t)$. In contrast to the linear simulations throughout which the base flow was frozen, the nonlinear simulation implicates an evolving base flow. In the linear stage of the evolution the perturbation $\boldsymbol{u}'(t)$ can be retrieved by the following approximation $\boldsymbol{u}_\epsilon(t) \simeq \boldsymbol{u}_{\epsilon=0}(t) + \epsilon\|\boldsymbol{U}\|\boldsymbol{u}'(t)$. An unperturbed flow ($\epsilon = 0$) is thus required in order to follow the evolution of the perturbation $\boldsymbol{u}'(t)$ and the perturbation kinetic energy $E'(t) = \|\boldsymbol{u}'(t)\|^2$ can then be computed as

$$E'(t) = \epsilon^{-2}\|\boldsymbol{U}\|^{-2}\|\boldsymbol{u}_\epsilon(t) - \boldsymbol{u}_{\epsilon=0}(t)\|^2. \tag{2.8}$$

3. Reference case: response to infinitesimal forcing of the linear optimal perturbation

The reference case for the nonlinear dynamics of the Crow instability is established for an infinitesimal initial perturbation amplitude to get as close to the linear limit as possible ($\epsilon \to 0$). This case can be assimilated to the far-field wake of an aircraft in very calm and homogeneous atmospheric conditions. The linear optimal perturbation is superimposed on the base flow with an initial amplitude $\epsilon = 10^{-3}$. It is important to

https://doi.org/10.1017/jfm.2016.176 Published online by Cambridge University Press

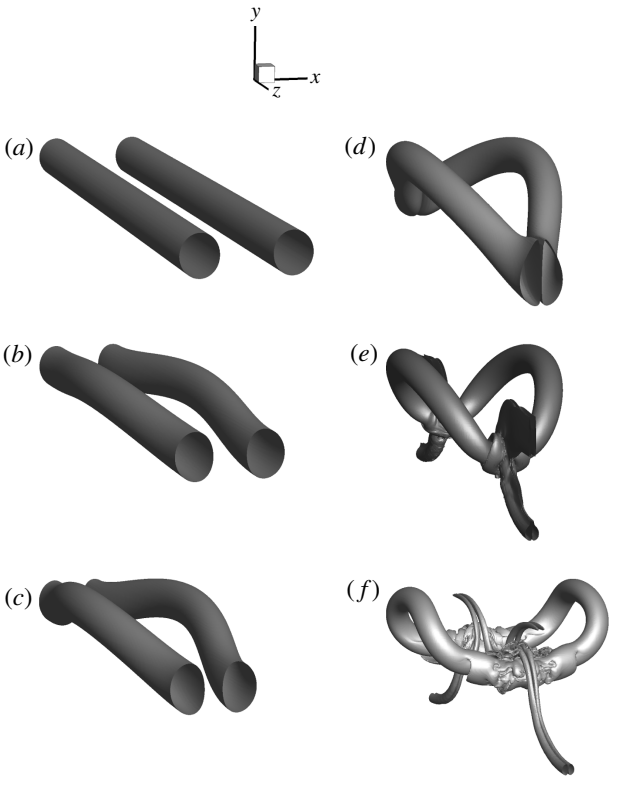

FIGURE 1. Isovorticity contours at 20 % of the initial maximum of vorticity $\omega = 0.2|\omega_{max}(t=0)|$ showing the initial development of the Crow instability and the linking of the vortices: (*a*) $t=0$; (*b*) $t=7$; (*c*) $t=8$; (*d*) $t=9$; (*e*) $t=10$; (*f*) $t=11$.

note that at such a small initial amplitude, the overall dynamics will be the same as if the flow was initialised with the most unstable Crow mode. The use of the linear optimal perturbation here has only one objective: accelerating the development of the instability to limit simulation time costs.

The dynamics of the vortex pair is concurrent with that described by Crow (1970). Isovorticity contours illustrate the dynamics in figure 1. As the simulations are carried out over one wavelength of the Crow instability, only one wavelength is shown. The vortices undergo a gradual symmetrical sinusoidal deformation with the cores remaining in a plane of angle approximately equal to 45° with respect to the spanwise direction (x). Eventually at time $t=9$ the closest parts of the vortices meet and are pressed together. The descent of the dipole and the continued deformation of the vortices creates a distinctive head–tail dipole shape in the connection z-planes. Vorticity cancellation between the opposite signed vortices becomes very strong in these areas, and the linking phenomenon is observed. This well-known event is described in more detail in the following paragraph. Once linking is complete, the vortices form a chain of vortex rings connected by thin vorticity threads. Due to the original symmetrical deformation of the vortices, the sides of the rings remain curved upwards, as can be observed at $t=11$.

Over recent years a great deal of attention has been paid to vortex linking because of its supposed involvement in turbulence cascade and turbulent noise generation.

https://doi.org/10.1017/jfm.2016.176 Published online by Cambridge University Press

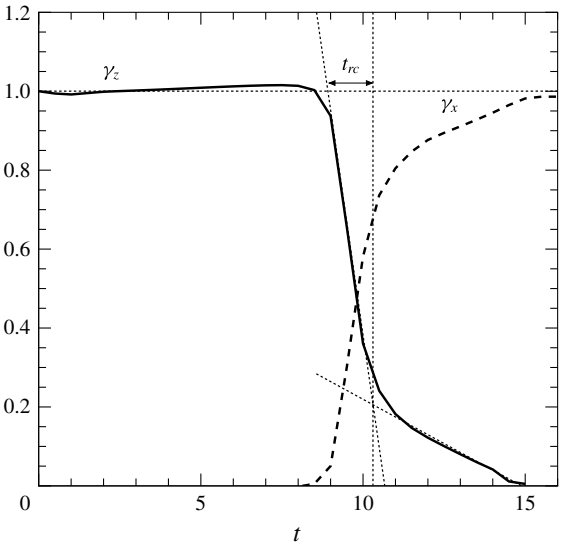

FIGURE 2. Evolutions of the circulation γ_z in the connection plane ($z = L_z/2$) and the circulation γ_x in the dividing plane ($x = 0$). Evidence of the transfer of axial vorticity to spanwise vorticity throughout the linking process.

In spite of a great number of analytical, numerical and experimental studies, some aspects of this complicated process are still unclear. Saffman (1990) developed a model describing the linking of two counter-rotating vortices and Moriconi (2000) extended the model into high Reynolds numbers. Detailed descriptions of the physical mechanisms at play are given by many authors (Melander & Hussain 1989; Marshall, Brancher & Giovannini 2001; Hussain & Duraisamy 2011). To summarise quickly, when the vortices touch, viscous diffusion causes the touching parts to cancel each other out. The remaining strands on the outer sides of the vortex cores then reconnect to form bridges joining the two vortices. These bridges become strong and move away from each other through self-induction, leaving behind the remnants of the original vortices in threads. The linking of the vortex pair into vortex rings can be observed particularly well when studying the evolution of the axial circulation γ_z in the connection z-plane ($z = \pm L_z/2$) and the spanwise circulation γ_x in the symmetry plane ($x = 0$), as can be seen in figure 2. These circulations are defined by the following expressions:

$$\gamma_z = \int_0^{L_x/2} \int_{-L_y/2}^{L_y/2} \omega_z(x, y, L_z/2)\, \mathrm{d}x\, \mathrm{d}y \tag{3.1}$$

$$\gamma_x = \int_{-L_y/2}^{L_y/2} \int_0^{L_z/2} \omega_x(0, y, z)\, \mathrm{d}y\, \mathrm{d}z, \tag{3.2}$$

with ω_x and ω_z the x- and z-components of the vorticity vector, respectively. Vorticity cancellation between the colliding counter-rotating vortices leads to a dramatic drop of the axial circulation γ_z from $t = 8$ to $t = 10$. At this point the threads linking the vortex rings are still present and so the decrease of the axial circulation slows before

https://doi.org/10.1017/jfm.2016.176 Published online by Cambridge University Press

finally reaching almost zero at around $t = 13.5$. From this point the axial circulation is nil, demonstrating that once the vortex rings are formed and the threads have disappeared, no axial vorticity exists in the $(z = L_z/2)$-plane. The spanwise circulation γ_x is negligible initially but from $t = 8$ increases rapidly, eventually attaining 98 % of the initial value of γ_z. The evolution of these quantities demonstrates the transfer of vorticity from the axial direction to the spanwise direction. Of the numerous ways to characterise this phenomenon, one of the most striking is the connection time t_{rc}. This corresponds to the duration between the vortex cores touching and the bridges separating. From pure observation of the connection progress, it is virtually impossible to determine a definitive connection time value. However Melander & Hussain (1989) and Leweke & Williamson (2011) noted that it is possible to deduce a value by inspecting the evolution of the circulation in the connection plane. Using the same method, illustrated in figure 2, the linking time in this case is found to be equal to $t_{rc} = 1.5 \pm 0.2$ compared with $t_{rc} = 0.7 \pm 0.1$ for Melander & Hussain (1989) at $Re = \Gamma/\nu = 1000$ and $t_{rc} = 0.9 \pm 0.2$ for Leweke & Williamson (2011) for $Re = \Gamma/\nu = 2340$. The error estimation of this type of method is around 15–20 %. The disparity between the connection time found here and those established in other papers is most certainly due to the difference in Reynolds number and the difference in axial perturbation wavelength. Although the aspect ratios used are very similar ($a/b = 0.18$ for Leweke and Williamson and $a/b = 0.22$ for Melander and Hussain) the axial wavelengths chosen for the deformation of the vortex pair are quite different: $\lambda_z/b = 5.13$ for Leweke and Williamson and $\lambda_z/b = 3.85$ for Melander and Hussain (as opposed to $\lambda_z/b = 7$ in the present study).

The subsequent evolution of the flow is analysed in the light of several quantities, namely the length-averaged axial circulation $\Gamma_z(t)$ and spanwise circulation $\Gamma_x(t)$ which indicate the strength of the vortices, the enstrophy $\xi(t)$ and the total kinetic energy $E(t)$. These quantities are expressed as integrals over the computational volume V:

$$\Gamma_z(t) = \frac{1}{L_z} \int_V \omega_z(t)\, \mathrm{d}V \tag{3.3}$$

$$\Gamma_x(t) = \frac{1}{L_x} \int_V \omega_x(t)\, \mathrm{d}V \tag{3.4}$$

$$\xi(t) = \frac{1}{2} \int_V \boldsymbol{\omega}(t)^2\, \mathrm{d}V \tag{3.5}$$

$$E(t) = \frac{1}{2} \int_V \boldsymbol{u}(t)^2\, \mathrm{d}V. \tag{3.6}$$

Figure 3(*a*,*b*) shows the evolution of these quantities in time. The evolution of the length-averaged circulations highlights the exchange of circulation between the axial and spanwise directions at the linking stage, and then again at $t = 15$ and $t = 24$. After linking, the maximum of length-averaged circulation $\max(\Gamma_x, \Gamma_z)$ remains at around 60 % of the initial value of Γ_z and is attained at $t \approx 13$ by Γ_x and $t \approx 19$ by Γ_z. This demonstrates the existence of a periodic behaviour that will be analysed further in the following paragraphs by observing the dynamics of the vortex rings. The nature of the flow can be examined by considering the evolution of the enstrophy ξ. The progression in time of the enstrophy is governed by

$$\frac{\partial \xi}{\partial t} + (\boldsymbol{u} \cdot \boldsymbol{\nabla})\xi - \nu \nabla^2 \xi = S_{\omega\omega}\xi - \nu \boldsymbol{\nabla\omega} : \boldsymbol{\nabla\omega}, \tag{3.7}$$

https://doi.org/10.1017/jfm.2016.176 Published online by Cambridge University Press

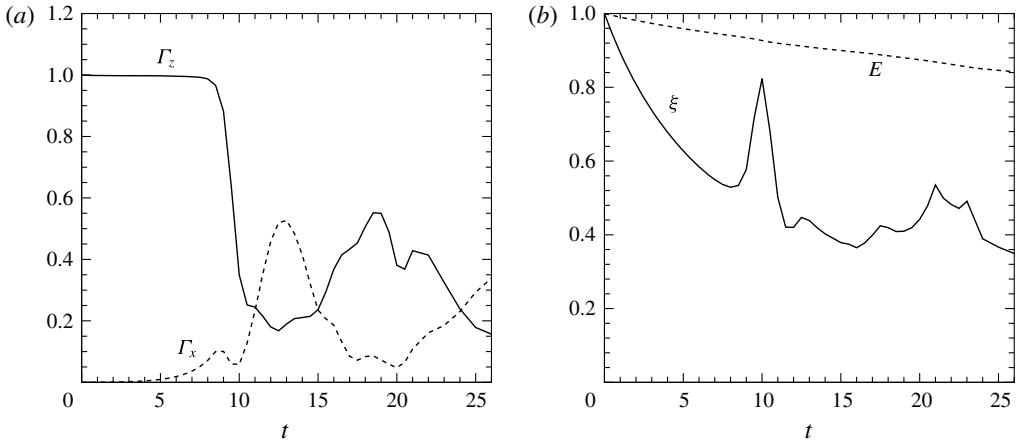

FIGURE 3. (*a*) Evolution of length-averaged axial and spanwise circulations Γ_z and Γ_x over time. (*b*) Total kinetic energy E and enstrophy ξ evolution over time. Note the kinetic energy and enstrophy were integrated over the whole domain whereas the circulations were integrated over half of the domain.

with $S_{\omega\omega} = 2[(\boldsymbol{n}_\omega \cdot \boldsymbol{\nabla})\boldsymbol{u}] \cdot \boldsymbol{n}_\omega$ the component of strain in the vorticity direction and $\boldsymbol{n}_\omega = \boldsymbol{\omega}/\|\boldsymbol{\omega}\|$. The left-hand side of the equation constitutes the advection–diffusion term, the first term of the right-hand side is the production term and the last term ensures viscous dissipation. Production of enstrophy occurs through stretching of vorticity. During the first stage of the evolution of the vortices, before the connection, the enstrophy decreases rapidly which can be expected in the case of a laminar flow. At $t = 10$ the linking process entails massive vorticity stretching which generates a large spike of enstrophy. The subsequent enstrophy peaks are due to the stretching of smaller structures formed around the vortex ring. Finally the kinetic energy of the flow decreases steadily over time as a consequence of viscous dissipation. This behaviour can be expected from a laminar viscous flow.

At the end of the linking process $t = 11$, the vortex rings produced are circular and the sides corresponding to the original straight vortices are curved upwards as a result of the Crow instability (see figure 1). Self-induced vorticity due to the curvature of the vortex draws these sides outwards (in the spanwise direction) until the ring is flat. The resulting rings are then elliptic with the major axis aligned in the spanwise direction. The dynamics of an elliptic vortex ring have been studied analytically by Arms & Hama (1965). Using the Biot–Savart law and adopting a localised-induction theory Arms & Hama (1965) established several principles that regulate the dynamics of elliptic vortex rings. They concluded that elliptic vortex rings experience periodic deformations, where the major and minor axes periodically exchange their orientations. The period T of this behaviour depends on the eccentricity $e = \sqrt{1 - l^2/L^2}$ of the original ellipse, where L is the length of the semi-major axis and l the length of the semi-minor axis. The greater the eccentricity, the more complex is the deformation. These results were validated numerically and experimentally by Dhanak & Bernardinis (1981).

An estimation for the initial eccentricity in this case is $e \approx 0.97$ with an axis ratio $l/L \approx 0.26$. The different stages of evolution of the vortex rings, illustrated in figure 4 with vorticity norm isocontours, are very similar to those described by Arms

https://doi.org/10.1017/jfm.2016.176 Published online by Cambridge University Press

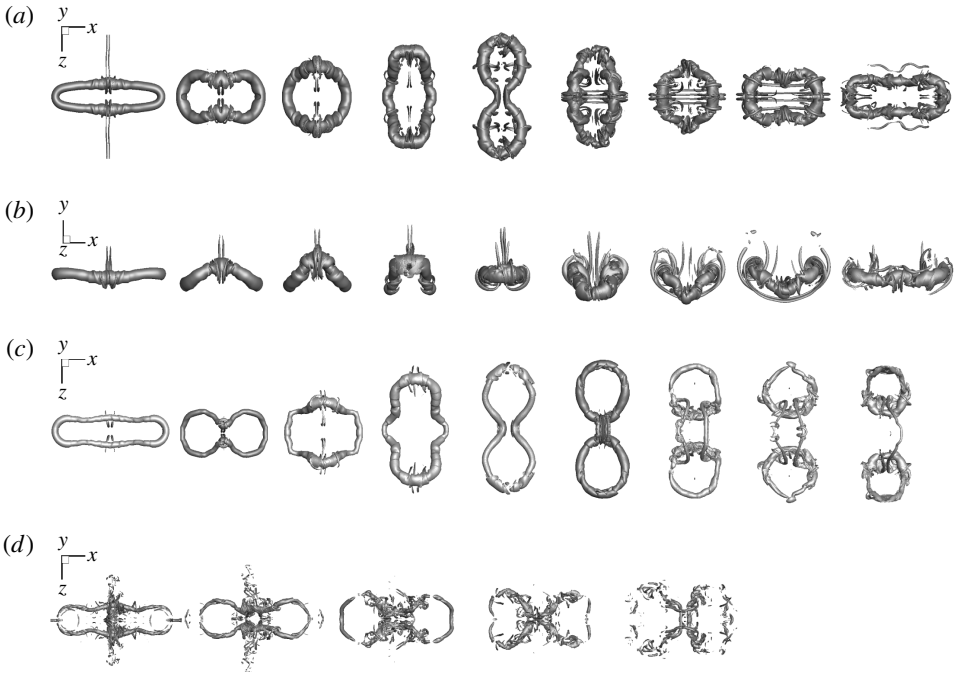

FIGURE 4. Vorticity isocontours at 14 % of the initial vorticity norm maximum $\omega = 0.14|\omega_{max}(t=0)|$ for $\epsilon = 10^{-3}$, $t = 13$, 15, 16, 17, 19, 22, 23, 24, 26 (*a*,*b*) and 20 % of the initial vorticity norm maximum $\omega = 0.2|\omega_{max}(t=0)|$ for $\epsilon = 10^{-2}$, $t = 7$, 9, 10, 11, 12, 13, 14, 15, 16.4 (*c*) and $\epsilon = 3 \times 10^{-2}$, $t = 7$, 8.2, 9, 10, 12 (*d*) evolution of the vortex rings during the first period T. View from above (*a*) and the front (*b*) for each stage of the $\epsilon = 10^{-3}$ case, view from above only for $\epsilon = 10^{-2}$ (*c*) and $\epsilon = 3 \times 10^{-2}$ (*d*).

& Hama (1965) and Dhanak & Bernardinis (1981), in particular the 'figure-of-eight' shape attained at the half-period $T/2$ (here at $t = 19$). The cores are very close in the centre of the domain at this time, but they do not touch enough for linking to occur and the deformation continues. Had the cores touched at this point, viscous diffusion would certainly have lead to the annihilation of vorticity between the parts of opposing sign and the vortices would have split once more into two smaller vortex rings. It is conceivable that another Crow wavelength, generating a different eccentricity, could lead to such a scenario. At time T the resulting ring is an ellipse of similar size and shape to the original ellipse.

By observing the movement of the vortex ring, the deformation period is estimated to be $T = 13$. Two complete periods are captured by the present simulation although only one is shown in figure 3. Using the expression of Arms & Hama (1965) derived by linearised analysis of a circular vortex ring and adapted to account for the eccentricity of the elliptic ring, the theoretical period of oscillation is $T_{th} = 10.4$, providing reasonable agreement with the simulated value. Such discrepancies between theory and simulation were also observed by Arms & Hama (1965): typically a 6 % difference for $e = 0.94$ and larger for increased eccentricity.

This behaviour of vortex rings issued from the linking of a vortex pair was observed experimentally by Leweke & Williamson (2011). They observed the successive

https://doi.org/10.1017/jfm.2016.176 Published online by Cambridge University Press

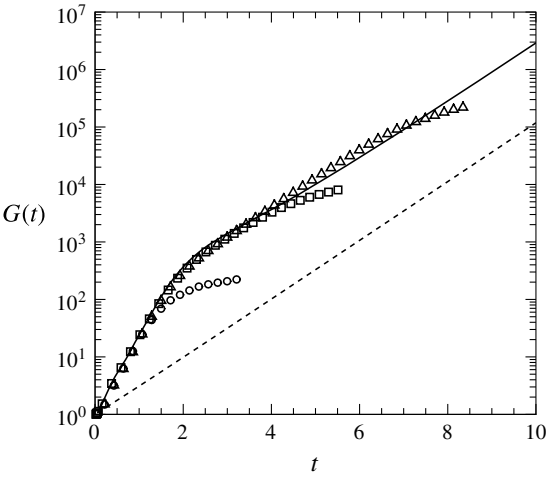

FIGURE 5. Perturbation energy growth rates for the linear evolution of the Crow instability eigenmode (dashed line) and the linear optimal perturbation (solid line), as well as those obtained for the evolution of the linear optimal perturbation initialised with $\epsilon = 10^{-3}$ (triangles), $\epsilon = 10^{-2}$ (squares) and $\epsilon = 3 \times 10^{-2}$ (circles).

deformations characteristic of elliptic vortex rings over less than a period, and in some cases a second reconnection of the vortex rings into longer ellipses resembling the initial straight vortices. The simulated results of this paper confirm the initial development described by Leweke & Williamson (2011) (stages A to E in their figure 14) but the second reconnection of the vortices is not retrieved.

These results indicate that when subjected to infinitesimal forcing, a pair of counter-rotating vortices go through multiple evolutions without losing much coherence over more than 25 characteristic times. Loss of coherence could not be reached in the simulated time frame meaning that in calm atmospheric conditions aircraft wakes may be present for durations longer than those required for vortex linking.

4. Nonlinear response to the linear optimal perturbation

In this section the nonlinear response to the linear optimal perturbation is analysed by a parametric study based on the initial perturbation amplitude ϵ. Figure 5 shows the perturbation energy growth $G(t)$ over time for two example values of ϵ as well as the infinitesimal case $\epsilon = 10^{-3}$ and the equivalent growths for the Crow eigenmode and linear optimal perturbation as outlined by Brion *et al.* (2007). The perturbation energy growth is defined as follows:

$$G(t) = \frac{E'(t)}{E'(0)}, \tag{4.1}$$

with E' the perturbation kinetic energy defined at (2.8). First note that all the perturbation energy growths initially follow the linear behaviour and then branch off, signalling at that moment the beginning of nonlinear behaviour. The recording of the perturbation energy growth is halted soon after the divergence from the linear behaviour as from that time the definition of the perturbation kinetic energy (2.8) is no longer valid. In the case of infinitesimal initial amplitude $\epsilon = 10^{-3}$ this occurs at $t \approx 8$ which coincides with the start of vortex linking, the first nonlinear event to

https://doi.org/10.1017/jfm.2016.176 Published online by Cambridge University Press

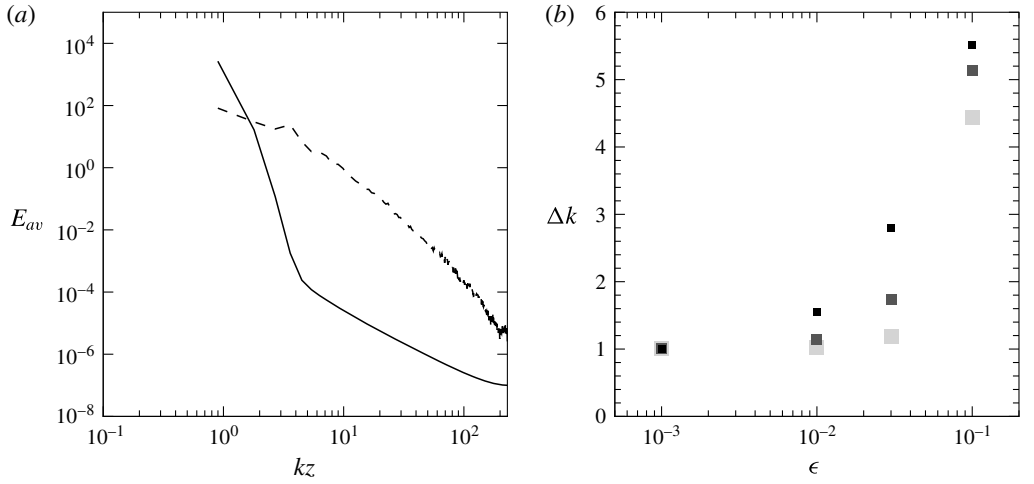

FIGURE 6. (*a*) Kinetic energy spectrum with $\epsilon = 10^{-3}$ (solid line) and $\epsilon = 3 \times 10^{-2}$ (dashed line) at $t = 3$; (*b*) spectrum width at $t = 1$ (light grey), $t = 2$ (grey) and $t = 3$ (black) for different initial amplitudes ϵ of the linear optimal perturbation.

occur. Increasing the initial amplitude simply shifts this scenario in time and generates the vortex linking sooner. However, for $\epsilon = 3 \times 10^{-2}$ the deviation from the linear behaviour occurs before the exponential perturbation energy growth characteristic of the Crow instability is even established. Therefore, a critical amplitude ϵ_c which distinguishes two behaviours can be defined such that $10^{-2} < \epsilon_c < 3 \times 10^{-2}$. For $\epsilon < \epsilon_c$ the Crow instability is reached before nonlinear effects come into play, whereas for $\epsilon > \epsilon_c$ nonlinear dynamics start during the initial transient growth due to the linear optimal perturbation.

An efficient way to measure the impact of nonlinear phenomena in an initially purely harmonic flow is to look at its wavelength composition. In the case of an infinitesimal perturbation, only the wavelength corresponding to the perturbation will experience growth over time. This is demonstrated in figure 6(*a*) which gives the volume-averaged energy spectrum of the $\epsilon = 10^{-3}$ and $\epsilon = 3 \times 10^{-2}$ cases at $t = 3$. For $\epsilon = 10^{-3}$ the majority of the energy is concentrated at wavenumber $kb = 0.9$ (the first peak in the spectrum) which corresponds to the wavelength of the initial perturbation (and that of the computational domain). However, as soon as the perturbation reaches sufficient amplitude, interactions of the perturbation with itself produce smaller scales, thus widening the spectrum as can be seen for $\epsilon = 3 \times 10^{-2}$. Here the Crow wavenumber $kb = 0.9$ is less amplified compared with the infinitesimal case. A gain of around 100 is obtained for $\epsilon = 3 \times 10^{-2}$ as opposed to about 2700 for $\epsilon = 10^{-3}$ as can also be seen in figure 5. Note that such important gains, which are much larger than those permitted by the Crow amplification, are made possible by the use of the adjoint mode as the initial perturbation.

The impact of the initial amplitude ϵ is analysed with the width of the energy spectrum Δk in the axial (z) direction, defined as

$$\Delta k = \frac{\int kE(k)\,\mathrm{d}k}{\int E(k)\,\mathrm{d}k}, \tag{4.2}$$

https://doi.org/10.1017/jfm.2016.176 Published online by Cambridge University Press

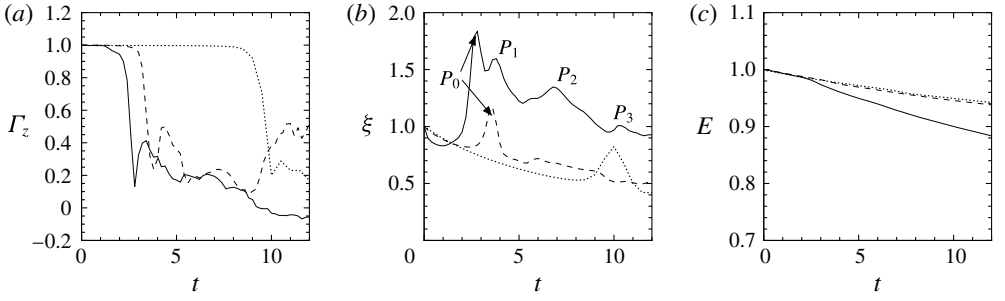

FIGURE 7. (*a*) Length-averaged axial circulation $\Gamma_z(t)$, (*b*) enstrophy $\xi(t)$ and (*c*) total kinetic energy $E(t)$ for $\epsilon = 10^{-2}$ (dashed lines), $\epsilon = 3 \times 10^{-2}$ (full lines) and $\epsilon = 10^{-3}$ (dotted lines) for comparison.

with $E(k)$ the total kinetic energy of the flow at the wavenumber k. Figure 6(*b*) shows the resulting spectrum widths for varying ϵ for $t = 1$–3. Only a few values of ϵ have been tested but they are sufficient to draw the conclusion that over a certain limit the nonlinear behaviour induced by the linear optimal perturbation is drastically different and leads to a rapid development of smaller-scale structures. The instant $t = 3$ is particularly interesting because at that time (see figure 5) either exponential Crow growth has been reached ($\epsilon < \epsilon_c$) or nonlinear behaviour has taken place ($\epsilon > \epsilon_c$).

Next, the effect of the initial amplitude on the length-averaged axial circulation, the enstrophy and kinetic energy is evaluated. Figure 7 gives the evolutions of these quantities through time for $\epsilon = 10^{-2}$ and $\epsilon = 3 \times 10^{-2}$ as well as $\epsilon = 10^{-3}$ for comparison.

The evolution of the length-averaged axial circulation Γ_z of the two simulations (see figure 7*a*) shows that raising the initial perturbation amplitude accelerates the displacement of the vortices and anticipates linking. For $\epsilon = 10^{-2}$ the same periodic evolution of the circulation as in the infinitesimal case can be observed after the drop due to connection. The vorticity isocontours of figure 4 confirm this behaviour. The elliptic ring shape is attained at around $t = 7$ and the deformation of the ring is the same as in the infinitesimal case. However there is a major difference at later times: after the 'figure-of-eight' pattern the ring slowly separates into two smaller rings. This case was also described by Dhanak & Bernardinis (1981) for rings of axis ratio l/L under 0.2. The axis ratio of the elliptic ring at $t = 7$ in this case is $l/L = 0.195$. The separation of the ring into two smaller rings occurs in a very similar manner to the first connection of the vortices. Such a doubling of the dominant longitudinal wavelength has been observed in previous works (Misaka *et al.* 2012, for example). For $\epsilon = 3 \times 10^{-2}$ the periodic behaviour stops soon after the first exchange between γ_z and γ_x. This occurs after the first growth of Γ_z at $t = 3$ in figure 7(*a*). Γ_z then slowly drops to around zero at $t \approx 9$ and eventually becomes negative, implying that the periodic ring state is halted and a completely different state is in progress. In fact, analysis of figure 4 shows that once the first elliptic ring shape is reached (at $t = 7$) the deformation of the ring is stopped and it slowly loses coherence and breaks up under the effect of the many small-scale structures that have developed around the ring over time.

Initially, the enstrophy in both simulations decreases. As before, considerable growth (see mark P_0 in figure 7*b*) occurs at times coinciding with the collision of

https://doi.org/10.1017/jfm.2016.176 Published online by Cambridge University Press

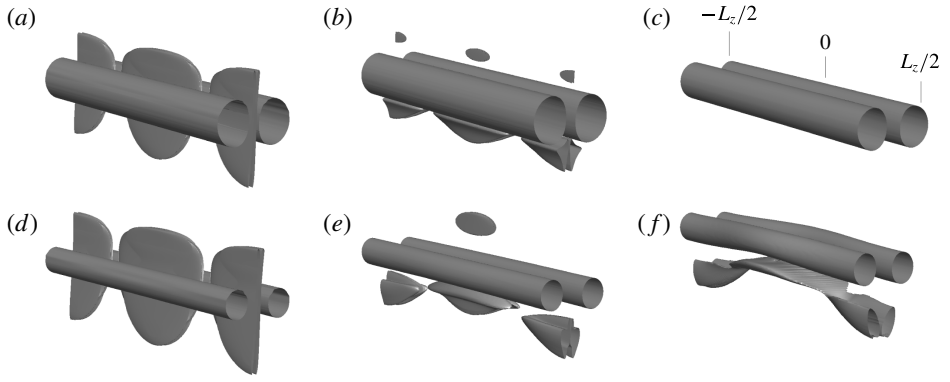

FIGURE 8. Initial vorticity contour evolution for (*a–c*) $\epsilon = 10^{-3}$ at $0.2\,\%\,|\omega_{max}(t=0)|$ (§ 3) and (*d–f*) $\epsilon = 3 \times 10^{-2}$ at $10\,\%\,|\omega_{max}(t=0)|$: (*a*,*d*) $t=0$, (*b*,*e*) $t=0.4$, (*c*,*f*) $t=0.85$.

the vortices, which involves massive vorticity stretching on the centreplane separating the two cores. Subsequently for $\epsilon = 10^{-2}$ the enstrophy decreases much more slowly and finally reaches the reference state $\epsilon = 10^{-3}$, meaning that no spectacular event occurs. However for $\epsilon = 3 \times 10^{-2}$ several peaks in enstrophy (P_0–P_3) occur after linking. Moreover, the final mean level of enstrophy remains much higher. This can be related to the persistence of small scales in the flow. The first peak (P_1), at $t \approx 3.8$ corresponds to the stretching of vorticity in the later stages of the linking phase, notably within the bridges and induced by the bridges on the remaining threads. This strongly nonlinear amplification has been observed by Melander & Hussain (1989), Marshall *et al.* (2001) and Hussain & Duraisamy (2011). Two other bumps (P_2 and P_3) occur at $t \approx 6.7$ and $t \approx 10$ which were absent in the low ϵ cases and which correspond to the encounter of opposite parts of the ring. Figure 7(*c*) gives the evolution of the kinetic energy of the flow. Up to $t \approx 2$ both cases see the kinetic energy decreasing at the same rate, which is about that of the linear perturbation $\epsilon = 10^{-3}$. However, linking in the case $\epsilon = 3 \times 10^{-2}$ promotes an increased decay which is not observed in the case $\epsilon = 10^{-2}$. This increased dissipation stems from the larger production of smaller scales.

5. Accelerated decay

The results presented in § 4 have demonstrated that for initial amplitudes greater than ϵ_c, the evolution of the flow is significantly changed compared with the reference evolution described in § 3. Most importantly the flow rapidly loses most of its coherence. The underlying physical mechanisms are described in the following paragraphs. Note that the formation of a pair of vortex rings from the initially single elliptic ring observed in the case $\epsilon = 10^{-2}$ and the subsequent evolution which, from our simulation results, remains strongly coherent, is not discussed in the present study.

According to figure 5 the evolution over the first characteristic time is linear, regardless of the perturbation amplitude. This is confirmed by comparing the development of the vorticity contours of figure 8 in the linear (*a*) and nonlinear (*b*) cases up to $t \approx 0.4$. Note that the contour level is chosen to be much lower for

https://doi.org/10.1017/jfm.2016.176 Published online by Cambridge University Press

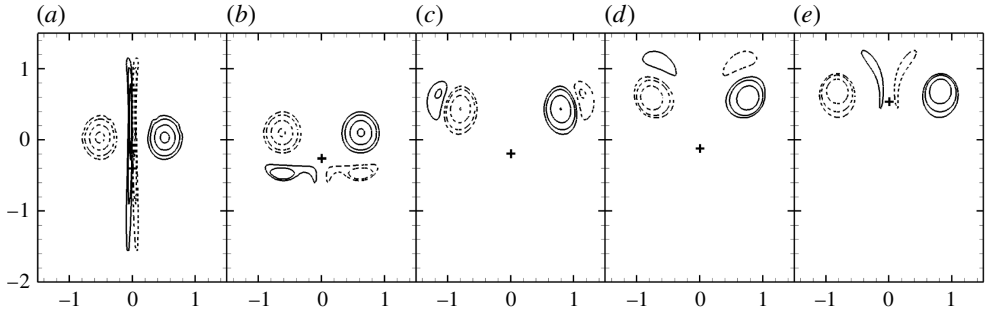

FIGURE 9. An (x, y)-plane slice of the axial vorticity at $z = 0$ at times $t = 0$ (*a*), 0.85 (*b*), 1.5 (*c*), 1.9 (*d*) and 2.4 (*e*). Here + gives the position of the leading hyperbolic point.

the $\epsilon = 10^{-3}$ case so that the perturbation can be seen. The perturbation sheets are amplified at the leading hyperbolic point and stretched horizontally beneath the cores, leading to the beginning of the vortex displacement. Details of this process are given by Brion *et al.* (2007). At $t = 0.85$ in the $\epsilon = 10^{-3}$ case (§ 3), the perturbation rapidly disappears whereas for $\epsilon = 3 \times 10^{-2}$ the initial perturbation energy is sufficient to resist viscous dissipation and becomes further involved in the vortex pair dynamics.

By definition, the perturbation is modulated at the Crow wavelength and therefore the vorticity sheets change sign every half-wavelength. The subsequent progression can be split into two domains: one in which the perturbation vorticity is of the same sign as the vortex in the corresponding half-domain ($x > 0$ or $x < 0$), and one in which the signs are opposite. When stretched at the leading hyperbolic point, the sheets become more compact and form vortex-like structures (see figure 8, $t = 0.85$) below the primary vortices. From this point, the flow can be viewed locally as a four-vortex type configuration, counter-rotating in $z \in [-L_z/4;\, L_z/4]$ and co-rotating in $z \in [-L_z/2;\, -L_z/4[\,\cup\,]L_z/4;\, L_z/2]$.

Figure 9 shows how axial vorticity evolves with time in a transverse (x, y)-plane at $z = 0$, the centre of the counter-rotating section. The secondary vortices are advected along the lower oval streamline and eventually tear away from the sheets. They are then drawn closer to the original vortices by 3D self-induction due to their horseshoe shape as shown in figure 10 at $t = 1.5$. The proximity between each original vortex and its opposite-signed secondary vortex encourages local dynamics on each side, that are added to the interaction between the original vortices. Mutual-induction between the newly formed dipoles pulls the original vortices upwards and outwards, exaggerating the sinusoidal deformation of the vortex cores as can be seen at $t = 1.5$. When the secondary vortices reach the top of the dipole, they are dragged into the downwash between the cores, and recommence their advection around the vortices ($t = 2.4$). Let Γ_2 and b_2 be the circulation and separation of the secondary vortices and Γ_1 and b_1 those of the primary vortices at $z = 0$. The ratio Γ_2/Γ_1 remains approximately constant in time such that $\Gamma_2/\Gamma_1 \approx -0.3$, and the distance ratio $b_2/b_1 \approx 1$. This matches the observation of Fabre, Jacquin & Loof (2002) for a counter-rotating vortex pair: the system is periodic, the vortices orbit around the vorticity centroids.

As can be observed in figure 10, at $t = 3.4$ the vortex cores present visible short-wave deformations. Those in the centre of the domain ($z/\lambda_z \in [-0.2, 0.2]$) result from the induction caused by the nearby secondary structures. To evaluate the scale of these

https://doi.org/10.1017/jfm.2016.176 Published online by Cambridge University Press

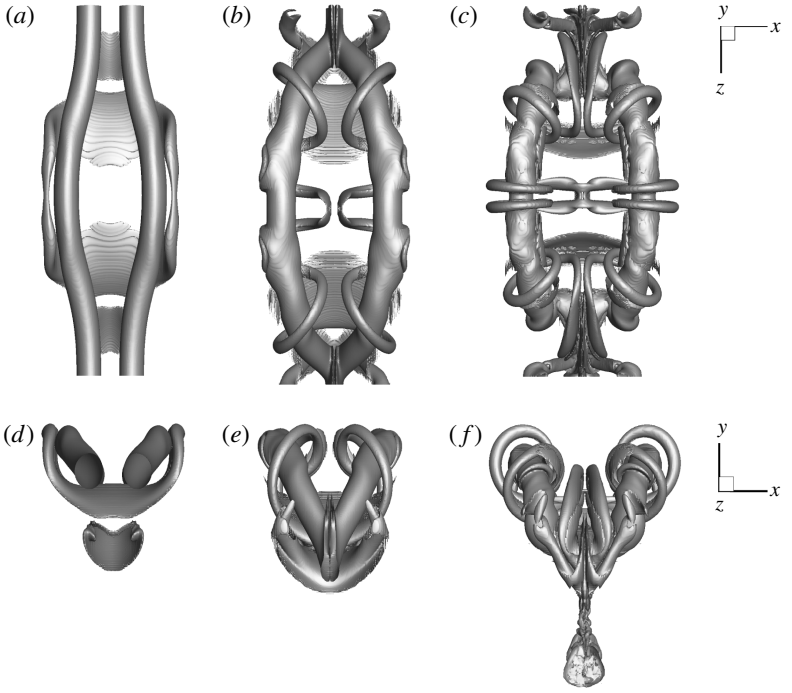

FIGURE 10. Vorticity isocontours at a value of 20 % $|\omega_{max}(t=0)|$ at (*a*,*d*) $t=1.5$, (*b*,*e*) $t=2.4$ and (*c*,*f*) $t=3.4$ for $\epsilon=3\times10^{-2}$.

deformations the axial evolution of the dispersion radius $\delta a(z)=(a(z)-\bar{a})/\bar{a}$ in this central region has been evaluated on each (x, y)-plane $S(z)$, with $a(z)$ calculated by

$$a(z)=\frac{\displaystyle\int_{S(z)} r\omega_z \,\mathrm{d}x\,\mathrm{d}y}{\displaystyle\int_{S(z)} \omega_z \,\mathrm{d}x\,\mathrm{d}y}, \tag{5.1}$$

with $r=((x-x_c)^2+(y-y_c)^2)^{1/2}$ and x_c and y_c the coordinates of the vortex core centre given by

$$x_c(z)=\frac{\displaystyle\int_{S(z)} x\omega_z \,\mathrm{d}x\,\mathrm{d}y}{\displaystyle\int_{S(z)} \omega_z \,\mathrm{d}x\,\mathrm{d}y} \tag{5.2}$$

$$y_c(z)=\frac{\displaystyle\int_{S(z)} y\omega_z \,\mathrm{d}x\,\mathrm{d}y}{\displaystyle\int_{S(z)} \omega_z \,\mathrm{d}x\,\mathrm{d}y} \tag{5.3}$$

https://doi.org/10.1017/jfm.2016.176 Published online by Cambridge University Press

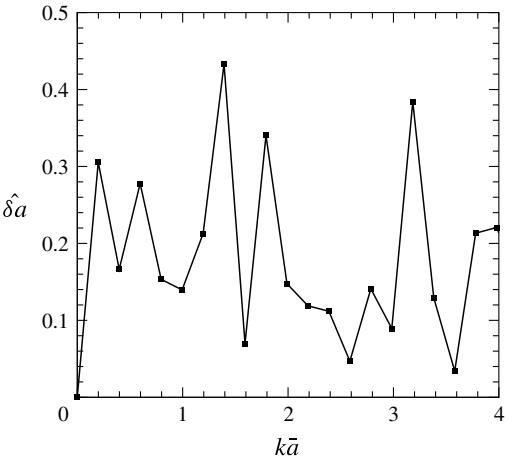

FIGURE 11. Fourier transform of the dispersion radius variation $\hat{\delta a}$ as a function of non-dimensional axial wavenumber $k\bar{a}$ at $t = 3.4$.

$\bar{a}$ is the average dispersion radius over the section studied:

$$\bar{a} = \frac{\int_{-0.2}^{0.2} a(z)\,\mathrm{d}z}{\int_{-0.2}^{0.2} \mathrm{d}z}. \tag{5.4}$$

External noise is filtered out by imposing a minimum vorticity of 10 % of the maximum vorticity in each section $S(z)$ in the calculations. Figure 11 gives the Fourier transform $\hat{\delta a}(k)$ of the variation of dispersion radius $\delta a(z)$ as a function of the non-dimensional wavenumber $k\bar{a}$. Several spikes can be seen, in particular for $k\bar{a} \approx 1.3$ which lies in the range of the optimal perturbation of an isolated vortex (Antkowiak & Brancher 2004). This suggests that the accelerated decay is additionally promoted by an optimal perturbation of the vortex cores.

Figure 12 gives the axial vorticity contours in the $z = L_z/2$-plane, the centre of the co-rotating section, which corresponds with the foreground plane of figure 10. The secondary vortices form a second counter-rotating dipole which moves downwards under the combined effects of the velocity field imposed by the primary vortices and of the self-advection between the perturbation vorticity. The separation distance ratio is $b_2/b_1 \ll 1$ and the behaviour is divergent which concurs with the aforementioned study of Fabre *et al.* (2002) except that here the perturbation vorticity diffuses before escaping the primary vortices. In return the secondary vortices induce a displacement of the primary structures towards one another, especially at instigation. This results in an increased 3D deformation of the vortices: the part of the vortices at $z = \pm L_z/2$ is drawn to the symmetry plane and downwards while, as mentioned earlier, the part at $z = 0$ is pulled away from the symmetry plane and upwards. This, in addition to the natural deformation of the vortices under the $m = 1$ Kelvin mode at the Crow wavelength, provokes the accelerated linking of the vortices. At $z = L_z/2$ the original cores are then pressed tightly together in a head–tail shape, ready for the connection of the vortices into rings at $t = 2.4$. The evolution of the location of the

https://doi.org/10.1017/jfm.2016.176 Published online by Cambridge University Press

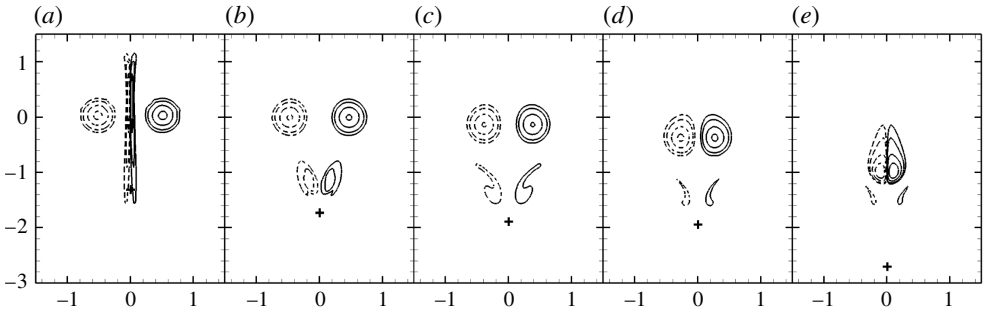

FIGURE 12. An (x, y)-plane slice of the axial vorticity at $z = L_z/2$ at times $t = 0$ (a), 0.85 (b), 1.5 (c), 1.9 (d) and 2.4 (e). Here + gives the position of the leading hyperbolic point.

leading hyperbolic point, shown in figures 9 and 12, also shows that the entire oval surrounding the recirculating flow around the vortices is modified in this process.

In addition to this analysis of the axial vorticity in two sectional planes, the map of vorticity contours in figure 10 demonstrates the appearance, in the long term, of smaller-scale variations in the flow. They are the remnants of the initial perturbation which were not present for lower values of ϵ. Observation of figures 10 and 4 shows that this added noise deteriorates into smaller scales through tilting and stretching, continuously forcing the primary vorticity, until the vortex ring finally breaks, at $t = 12$.

6. Conclusion

This paper has reported on the long-term evolution of the Crow instability in a homogeneous and turbulence-free environment. A pair of Gaussian vortices is perturbed by the most amplified perturbation of the Crow instability, the adjoint mode, introduced with various initial amplitudes. When subjected to an infinitesimal initial perturbation, the vortices undergo a series of transformations: the linear Crow stage, linking and the formation of vortex rings. The ensuing stage of evolution is found to be a periodically evolving ring state. While such a phenomenon was known to occur in elliptic vortex rings, it is the first time that its manifestation in the evolution of wake vortices is demonstrated. This result was obtained by pursuing the flow computation for an unusually long time. From an application point of view this demonstrates that aircraft wake vortices may last a great deal longer than would be expected. For instance Spalart (1998) determined that the typical lifespan of an aicraft wake is around five or six characteristic times. Such data is acquired usually from Lidar measurements of wake vortices conducted from the ground. The disparity between that and the lifespan obtained in this present analysis may lie in the possible inability of Lidar to measure vortex rings due to the complexity of such flows and the constraints of Lidar measurement (namely volume integration and projection of the flow velocity along the laser beam). The relatively low Reynolds number and large initial aspect ratio of the vortices in the present study are thought not to reduce the scope for application, as observation of actual aircraft wakes show practically identical initial dynamics.

The adjoint mode of the Crow instability is evaluated as a solution to prevent the periodic ring state. While the adjoint is the initial perturbation that triggers the largest

https://doi.org/10.1017/jfm.2016.176 Published online by Cambridge University Press

Crow instability growth, its potential to disrupt the flow in the stages following the linking of the vortices was unknown. Also, were it indeed possible, the cost required to do this effectively needed to be identified. Varying the initial perturbation amplitude from that used for the reference state described in § 3 to larger, yet still low values, showed the existence of a threshold distinguishing two behaviours. This threshold corresponds to a perturbation of about 3 % in relative amplitude compared with the background flow. When subjected to a perturbation of amplitude higher than the threshold, the development of the periodic ring state is stopped at the beginning of the first period. The once coherent vortical structures transform into small incoherent vortices that, if the simulation could have been pursued longer, would certainly have initiated the turbulent cascade. The physics of this process were analysed in detail, showing that the flow dynamics split into two regions per wavelength in the longitudinal direction, depending on the interaction of vorticity sign between the primary vorticity and the perturbation. Each zone could be likened locally to a four-vortex-type configuration, that promotes local induction phenomena and increases the initial deformation of the vortices, resulting in an accelerated linking. In addition, it is suggested that the remnants of the adjoint mode perturbation, that wrap around the vortices, trigger a single-vortex-type optimal perturbation in each individual vortex. Overall these additional dynamics lead to a considerable reduction of the vortices' lifespan, since they are seen to disintegrate after only 13 characteristic times.

Whilst evidently the dynamics of a vortex pair is particularly resilient to initial forcing, the present analysis also shows that large structural variations can take place. The varying parameter here was the initial perturbation amplitude ϵ. By increasing ϵ from 10^{-3} to 10^{-2} the flow eventually evolved into a sequence of two vortex rings per Crow wavelength, thus doubling the initial spatial periodicity of the wake. These differences compare well with documented vortex ring dynamics. Such disparity in the evolution of the flow raises new questions concerning the sensitivity of wake vortices to external parameters and should act as strong motivation for further analysis.

Acknowledgement

This work was performed using HPC resources from GENCI-IDRIS (grant 2014-i20142a7323).

REFERENCES

ANTKOWIAK, A. & BRANCHER, P. 2004 Transient energy growth for the Lamb–Oseen vortex. *Phys. Fluids* **16** (1), L1–L4.

ARMS, R. J. & HAMA, F. R. 1965 Localized-induction concept on a curved vortex and motion of an elliptic vortex ring. *Phys. Fluids* **8** (4), 553–559.

BRION, V., SIPP, D. & JACQUIN, L. 2007 Optimal amplification of the Crow instability. *Phys. Fluids* **19** (11), 111703.

CROW, S. C. 1970 Stability theory for a pair of trailing vortices. *AIAA J.* **8** (12), 2172–2179.

DHANAK, M. R. & DE BERNARDINIS, B. 1981 The evolution of an elliptic vortex ring. *J. Fluid Mech.* **109**, 189–216.

FABRE, D., JACQUIN, L. & LOOF, A. 2002 Optimal perturbations in a four-vortex aircraft wake in counter-rotating configuration. *J. Fluid Mech.* **451**, 319–328.

FARRELL, B. F. 1988 Optimal excitation of perturbations in viscous shear flow. *Phys. Fluids* **31** (8), 2093.

FISCHER, P. F., LOTTES, J. W. & KERKEMEIER, S. G. 2008 nek5000 Web page http://nek5000.mcs.anl.gov.

https://doi.org/10.1017/jfm.2016.176 Published online by Cambridge University Press

FONTANE, J., BRANCHER, P. & FABRE, D. 2008 Stochastic forcing of the Lamb–Oseen vortex. *J. Fluid Mech.* **613**, 233–254.

HUSSAIN, F. & DURAISAMY, K. 2011 Mechanics of viscous vortex reconnection. *Phys. Fluids* **23** (2), 021701.

HUSSAIN, F., PRADEEP, D. S. & STOUT, E. 2011 Nonlinear transient growth in a vortex column. *J. Fluid Mech.* **682**, 304–331.

LEWEKE, T. & WILLIAMSON, C. H. K. 2011 Experiments on long-wavelength instability and reconnection of a vortex pair. *Phys. Fluids* **23** (2), 024101.

MARSHALL, J. S. & BENINATI, M. L. 2005 External turbulence interaction with a columnar vortex. *J. Fluid Mech.* **540**, 221.

MARSHALL, J. S., BRANCHER, P. & GIOVANNINI, A. 2001 Interaction of unequal anti-parallel vortex tubes. *J. Fluid Mech.* **446**, 229–252.

MELANDER, M. & HUSSAIN, F. 1993 Coupling between a coherent structure and fine-scale turbulence. *Phys. Rev.* E **48** (4), 2669.

MELANDER, M. V. & HUSSAIN, F. 1989 Cross-linking of two antiparallel vortex tubes. *Phys. Fluids* **1** (4), 633–636.

MISAKA, T., HOLZPFEL, F., HENNINGSON, I., GERZ, T., MANHART, M. & SCHWERTFIRM, F. 2012 Vortex bursting and tracer transport of a counter-rotating vortex pair. *Phys. Fluids* **24** (2), 025104.

MIYAZAKI, T. & HUNT, J. C. R. 2000 Linear and nonlinear interactions between a columnar vortex and external turbulence. *J. Fluid Mech.* **402**, 349–378.

MORICONI, L. 2000 Vortex reconnection as the dissipative scattering of dipoles. *Phys. Rev.* E **61** (3), 2640.

POPE, S. B. 2000 *Turbulent Flows*. Cambridge University Press.

PRADEEP, D. S. & HUSSAIN, F. 2006 Transient growth of perturbations in a vortex column. *J. Fluid Mech.* **550**, 251–288.

SAFFMAN, P. G. 1990 A model of vortex reconnection. *J. Fluid Mech.* **212**, 395–402.

SCHMID, P. J. & HENNINGSON, D. S. 2001 *Stability and Transition in Shear Flows*. Springer.

SHAEFFER, N. & LE DIZÈS, S. 2010 Nonlinear dynamics of the elliptic instability. *J. Fluid Mech.* **646**, 471–480.

SIPP, D. 1999 Instabilités dans les écoulements tourbillonnaires. PhD thesis, Ecole Polytechnique, France.

SPALART, P. R. 1998 Airplane trailing vortices. *Annu. Rev. Fluid Mech.* **30** (1), 107–138.

https://doi.org/10.1017/jfm.2016.176 Published online by Cambridge University Press